Article

Nanopore Structure and Multifractal Characteristics of Continental Shale Oil Reservoir: A Case Study from Ziliujing Shales in the Sichuan Basin

Youzhi Wang [1], Wei Li [2,3,*], Xiandong Wang [1], Zhiguo Wang [1], Weiqi Ma [1], Yanping Zhu [1], Mengdi Sun [2,3,*], Bo Liu [2,3], Lijuan Cheng [2,3] and Xiaofei Fu [2,3]

[1] Exploration and Development Research Institute, PetroChina Daqing Oilfield Company Limited, Daqing 163712, China; wangyouzhi@petrochina.com.cn (Y.W.); wangxd2004@petrochina.com.cn (X.W.); scv1977@petrochina.com.cn (Z.W.); maweiqi@petrochina.com.cn (W.M.); zhuyanping@petrochina.com.cn (Y.Z.)
[2] Key Laboratory of Continental Shale Hydrocarbon Accumulation and Efficient Development, Northeast Petroleum University, Ministry of Education, Daqing 163318, China; liubo@nepu.edu.cn (B.L.); chenglijuan211@163.com (L.C.); fuxiaofei2008@sohu.com (X.F.)
[3] Institute of Unconventional Oil & Gas, Northeast Petroleum University, Daqing 163318, China
*   Correspondence: pingyaoliwei@nepu.edu.cn (W.L.); sunmd@nepu.edu.cn (M.S.)

Abstract: Thermal maturity of the shales from the Ziliujing Formation of the Jurassic age in the Sichuan Basin is in the hydrocarbon generation window, which makes it a candidate for shale oil and gas development. The meso- and macropore characteristics and heterogeneity of shales are important factors affecting the occurrence and development of oil and gas. However, the meso- and macropores of the Ziliujing shales have not been systematically studied. Thus, the mineral compositions and total organic carbon (TOC) of samples from this formation, as well as its pore structure, are analyzed by low-temperature N_2 adsorption technique. Moreover, the heterogeneity of the pores was determined by multifractal analysis. The results show that the Ziliujing shales can be classified into three types according to the distributions of mineral compositions of carbonate and mixed and argillaceous shales. Results revealed that the smallest meso- and macropore volume (PV), the smallest specific surface area (SSA), and the largest average pore diameter (APD) occur in the carbonate shales. However, the largest PV and SSA and the smallest APD are observed in the argillaceous shales. The porosity of carbonate shales is mainly concentrated between 5 nm and 30 nm. Compared with carbonate shales, the porosity with pore sizes less than 30 nm of mixed and argillaceous shales shows a rapid increase. Furthermore, inorganic minerals are the main factors affecting the pore distributions, while TOC shows a weak effect. Herein, clay minerals significantly increase the mesopore volume and the pore number with a size of less than 30 nm. The D_q-q curves reveal that the meso- and macropore distributions of Ziliujing shales show multifractal behavior, but the multifractal characteristics of pores of various shales are distinctly different. The information dimension D_1, the Hurst exponent H, and the width of the right side D_0–D_{10} are key indicators to distinguish the local variations within the pore structure of different types of shales. The carbonate shales have the largest multifractal spectra width and the smallest D_1 and H, while the opposite trend is found for the argillaceous shales. Clay minerals reduce the heterogeneity of the meso- and macropore distributions and increase the pore connectivity. Nevertheless, the carbonate minerals exhibit a reverse trend. Finally, it was found that TOC does not impact pore complexity as much. Collectively, this study supports our understanding of the occurrence of shale oil within various reservoir facies, thereby providing a guideline for future explorations in the Ziliujing Formation of the Jurassic age in the Sichuan Basin.

Keywords: Sichuan Basin; shale oil and gas; nanopores; low-temperature gas adsorption; multifractal analysis

1. Introduction

Recent advancements in technology have accelerated exploration and production from continental and lacustrine shale oil reservoirs in China [1–3]. The recoverable resource potential of shale oil in China is estimated at 34.98×10^8 t, which offsets the shortage of China's crude oil storage [4]. Large continental shale oil resources have been discovered in the Songliao, Ordos, Junggar, and Bohai Bay Basins [5]. As for the mentioned basins, significant achievements in occurrence, geological characteristics, sweet spot evaluation, and development technologies of shale oil reservoirs have been obtained [6–10]. Recently, several sets of organic-rich black shales with thermal maturity ranging from 1.3% to 1.5% in the Ziliujing Formation of the Jurassic age in the Sichuan Basin have been discovered [11]. The thermal maturity of the Ziliujing shale oil reservoir is in the oil and gas window, which shows great potential for shale oil and gas production. At present, the research regarding the Ziliujing shale reservoir is focused on the analysis of the main controlling factors of hydrocarbon enrichment [12,13]. Herein, shale oil reservoirs are considered to be fine-grained sediments with a wide range of pore sizes (nm to μm) and ultralow porosity [14]. The nanopores, including meso- and macropores, are important channels for shale oil occurrence and diffusion, which are important parameters to decide the future development of shale oil [15]. Therefore, systematic research on the meso- and macropore characteristics of the Ziliujing shales is needed.

Various methods have been reported to study pore characteristics of shale oil and gas reservoirs [16–21]. Jiang et al. [22] studied the pore characteristics of lacustrine shales with vitrinite reflectance (R_o) of 0.68–1.02% in the Ordos Basin through low-temperature nitrogen (N_2) adsorption (LNA) and high-pressure mercury intrusion porosimetry (MIP). They concluded that mesopores (2–50 nm) mainly controlled the distributions of pore volume and specific surface area of shales, and clay mineral contents and R_o were the main factors controlling pore development. Zhao et al. [23] employed small-angle neutron scattering, and fluid invasion methods were adopted to characterize the pore structure of typical American shale oil reservoirs. They found that large amounts of inaccessible porosity at pore size <10 nm occurred in typical American shales. Zhang et al. [24] analyzed the pore size distributions of shale oil reservoir samples from Dongying Sag, Bohai Bay Basin, by using LNA, scanning electron microscopy (SEM), MIP, and nuclear magnetic resonance (NMR) techniques. The results showed that a wide range of pore sizes with small-scale throats from nanometers to millimeters existed in shale oil reservoirs. Hou et al. [25] investigated the influences of clay minerals on the pore structure of lacustrine shales by SEM. They found that the type, occurrence, and composition of clay minerals are the key factors affecting pore characteristics. The results revealed that the pore-filling clay minerals, as well as layered ones, played a negative role in the pore development of lacustrine shales. Zheng et al. [26] characterized the multi-scale pore structure of tight shale oil reservoirs from the Triassic Yanchang Formation, Ordos Basin, by combining LNA, MIP, helium pycnometry, field emission scanning electron microscopy (FE-SEM), and nano-CT. They found that the pore sizes of the studied shales varied from 2 nm to >20 μm, but the dominant pores were in the range of 20–100 nm. Among these methods, the LNA technique is simple and convenient and has been widely used to characterize nanopore characteristics of shales [27,28]. Despite the popularity of this method, the evaluation of the nanopore structure of Ziliujing shales by the LNA method has not been carried out so far.

The pore heterogeneity or complexity is another critical parameter affecting the flow characteristics of fluids within pores of shales [29–31]. However, the traditional Euclidean geometry theory makes it difficult to characterize pore complexity [32]. Thus, fractal theory provides a scientific tool to quantitatively describe the complexity of the pore system by fractal dimension [33–35]. The pore size distributions of shales show fractal characteristics, but the pores with different size ranges exhibit multiple fractal characteristics [36]. The multifractals, described as an extension of single fractals, decompose self-similar measures into intertwined fractal subsets that can characterize the local complexity of measured variables [37]. Thus, in comparison with single fractal, multifractal can better explain

the local and differential distributions of the pore structure of shales with an acceptable accuracy [38]. Currently, limited research has been carried out in applying the multifractal approach to analyze the pore heterogeneity of shale oil reservoirs [39,40]. Liu et al. [41] applied multifractal methods to analyze gas adsorption isotherms for meso- and macropore and micropore heterogeneity of the Bakken shale. Their results showed that clay and organic matter reduced micropore complexity but increased meso- and macropore complexity. Likewise, Liu et al. [42] investigated multifractal characteristics of the pore structure of Middle Bakken based on FE-SEM image. They found that the heterogeneity of entire pores in images weas larger than that of the sub-pore groups in the same image. Zhang et al. [43] applied multifractal analysis on the samples that were polished by the ion beam via scanning electron microscopy to quantify the heterogeneity of major pores of shale oil reservoirs from Dongying Sag, Bohai Bay Basin. They reported that the interparticle pores possessed major complexity of pore morphologies and the simplest pore structure, while the dissolution pores had the simplest pore morphologies but had the most complex pore distributions. Guan et al. [44] conducted a multifractal analysis of N_2 adsorption and Hg pore size distributions of lacustrine shales from Cangdong Sag, Bohai Bay Basin. The results revealed that the pore distributions obtained from LNA are more homogeneous than those obtained from MIP, which implied that the pores with larger diameters could increase the heterogeneity of pore distributions. In this regard, the thermal maturity (R_o) of shale oil reservoirs described above is mostly less than 1.05%. Nevertheless, the R_o of the shale oil reservoirs in some basins in China is measured over 1.05%. However, the investigation on the multifractal characteristics of nanopore structure of shale oil reservoirs with medium to high thermal maturity (1.05% < R_o < 2.0%) is scarce, which may limit a better understanding of shale oil occurrence with R_o > 1.05%. In this case, the R_o values of the Ziliujing shale oil reservoirs mostly vary from 1.3% to 1.5%, and the research on the multifractal heterogeneity of nanopores from N_2 adsorption of this reservoir has not been reported. Hence, this study can help us to understand the occurrence of hydrocarbons and support exploration efforts within reservoirs with R_o > 1.05% in general.

In this paper, the lacustrine shale samples with different depths from the Ziliujing Formation in the Sichuan Basin were investigated. The aims are to (1) investigate the meso- and macropore characteristics, including pore volume (PV), specific surface area (SSA), and pore size distributions of shales by low-temperature N_2 adsorption; (2) analyze the effects of mineral compositions and total organic carbon (TOC) on meso- and macropore structures of different types of shales within this formation; (3) address the heterogeneity of meso- and macropore distributions by multifractal theory and discuss the governing factors on meso- and macropore heterogeneity. This research should be beneficial for more successful exploration and development of shale oil in the Ziliujing Formation of the Jurassic age in the Sichuan Basin.

2. Experiments and Methods

2.1. Sample Preparation

The shale samples were collected from drill cores of the Ziliujing Formation of the Jurassic age in the Sichuan Basin, with details listed in Table 1. The depth of the samples varies in the range of 1866.5–2017.0 m. Details about the geological settings of the study area and this formation can be found in our previous study [45]. To better address the meso- and macropore characteristics, a schematic diagram has been presented in Figure 1. First, the studied shale samples were grinded to measure TOC, and inorganic mineral compositions were determined via LECO test and X-ray diffraction (XRD) analysis, while meso- and macropore parameters were obtained by LNA. Then, the roles of TOC and mineral compositions on pore distributions of the studied shale samples were investigated. Finally, the heterogeneity of meso- and macropore distributions of different shale samples was studied by using multifractal theory. Moreover, major identified facies in the samples were chosen for more detailed analysis by quantitative evaluation of minerals through scanning electron microscopy (QEMSCAN).

Table 1. Depths and mineral compositions of shale samples.

Samples	Depth (m)	TOC (%)	Mineral Contents (%)							
			Q	FS	PC	CA	SR	PY	MC	CL
Dn9	1866.5	1.138	18.1	1.6	2.3	53.8	0.6	3.8	1.2	18.6
D97	2006.9	0.396	16.2	1.3	2.1	57.9	0.4	2.1	1.0	19.0
D62	1997.4	1.646	29.2	1.6	2.6	29.6	1.0	5.8	1.2	29.0
D123	2014.7	1.011	27.8	0.0	1.8	35.3	2.7	3.4	0.8	28.2
D130	2016.6	0.744	30.7	2.0	2.9	28.8	0.9	4.5	0.7	29.5
D132	2017.0	1.889	30.1	2.1	3.9	26.9	1.0	5.0	1.5	29.5
Dn17	1890.5	0.427	26.8	2.5	3.8	2.4	1.4	5.1	1.9	56.1
D17	1983.9	1.459	25.2	2.6	4.9	2.4	1.3	2.4	2.2	59.0
D26	1986.8	0.731	29.6	3.1	3.4	2.0	0.6	4.0	1.3	56.0
D71	1999.7	2.417	27.6	2.0	4.0	4.6	1.6	7.2	1.8	51.2
D80	2002.8	1.719	26.3	2.8	4.1	3.7	3.3	2.5	1.6	55.7
D91	2005.6	1.843	30.7	2.7	4.3	1.1	1.4	2.1	2.7	55.0

Note: Q—quartz; FS—feldspar; PC—plagioclase; CA—calcite; SR—siderite; PY—pyrite; MC—muscovite; CL—clay.
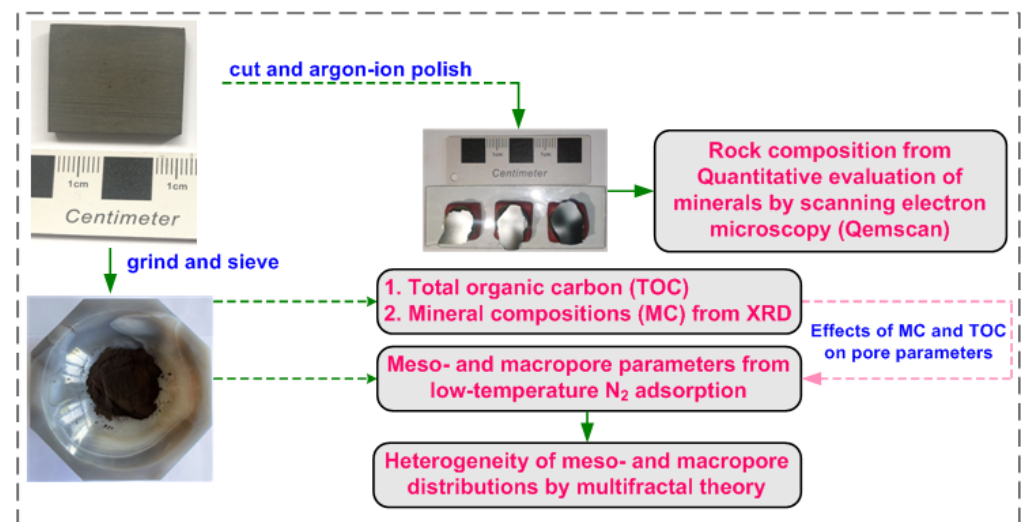

Figure 1. Schematic diagram for this study on the Ziliujing shale samples.

2.2. TOC Measurement, XRD Analysis, and QEMSCAN

The organic content and inorganic mineral compositions of the shale samples were characterized by TOC and XRD, respectively. The TOC of the shale samples was determined according to the GB/T 19145-2003 standard [46]. Based on SY/T 5163-2018 [47], the inorganic mineral compositions of the shale samples were determined by using a Japanese RIKEN SmartLab X-ray diffractometer. Before the experiment, the shale samples were grinded to a particle size >200 mesh using an agate mortar. The XRD experiments were performed at 40 kV and 200 mA, and the scanning range of minerals varied from 3° to 80° with a step size of 0.02°. A Quanta 650 equipment of FEI Company was chosen to conduct QEMSCAN analysis following the standard SY/T 6189-2018 [48]. Before the QEMSCAN, the shale samples were polished by an argon ion beam for 4 h to achieve a proper surface roughness of 1 μm in a scanning area of 1.5 × 1.5 mm^2.

2.3. Low-Temperature Nitrogen Adsorption Measurements

In this work, the pore size ranges of macropore and mesopore were determined according to the IUPAC classification [49], which has been broadly used in the pore characterization of coals and shales [27,30,36]. Thus, the pore sizes of macropore and mesopore were >50 nm and 2–50 nm, respectively. The meso- and micropore parameters were analyzed using a fully automatic specific surface analysis tester (ASAP 2460, Micromeritics,

Norcross, GA, USA). The N_2 at 77 K as a molecular probe was chosen to detect the pore characteristics of the shale samples. Before the experiments, the shale samples were placed in a vacuum drying oven and were dried at 110 °C for 12 h to remove the residual moisture and gas from the samples. The relative pressure (P/P_0) of the low-temperature N_2 adsorption/desorption isotherm was between 0.019 and 0.995. Based on the low-temperature N_2 adsorption/desorption curves, the specific surface area (SSA) and pore volume (PV) of the shale samples were obtained by the BET model and BJH model, respectively. The pore size distribution was obtained based on the DFT model, and the average pore diameter (APD) was obtained by the BJH model.

2.4. Multifractal Analysis

The multifractal singularity spectrum (α-$f(\alpha)$) and generalized dimensional spectrum (q-D_q) are equivalent to multifractal descriptions [50]. In this paper, relatively simple q-D_q spectra were used to characterize the pore heterogeneity of the shale samples [51]. As suggested by the work of Caniego et al. [52], the relative pressure P/P_0 is taken as the interval J, and the interval J of length L is divided into $N(\varepsilon) = 2^k$ boxes of scale ε based on the dyadic scaling down. In order to allow the smallest subinterval to contain measured pore volumes, the k values derived from low-temperature N_2 adsorption were from 0 to 3. The generalized dimensional spectra require the determination of four functions: mass probability $p_i(\varepsilon)$, partition function $\chi(q, \varepsilon)$, mass exponent $\tau(q)$, and generalized fractal dimension D_q.

(1) The probability mass distribution $p_i(\varepsilon)$ is the key to multifractal analysis to define a mass probability at different scales. These components will help to quantitatively characterize the local features of the pore volume distribution [53] and is defined in each box as:

$$p_i(\varepsilon) = \frac{N_i(\varepsilon)}{N_t} \tag{1}$$

where N_i is N_2 adsorption amount of the ith (i = 1, 2, 3...) box, and N_t is the total N_2 adsorption amount.

(2) The partition function $\chi(q, \varepsilon)$ can be calculated from $p_i(\varepsilon)$ function by using:

$$\chi(q, \varepsilon) = \sum_{i=1}^{N(\varepsilon)} p_i^q(\varepsilon) \tag{2}$$

where q is the order of statistical moments in the range of $[-\infty +\infty]$. In this paper, q varies from -10 to 10. When $q \gg 1$, the information on the high probability of pore volume is amplified [50]. When $q \ll -1$, the information on the low probability of pore volume is amplified [34]. Therefore, the multifractal method divides the pore volume with different pore sizes into local high- or local low-porosity regions.

(3) The mass exponent $\tau(q)$ for fractals is a power law relationship between $\chi(q, \varepsilon)$ and ε [52]:

$$\chi(q, \varepsilon) \propto \varepsilon^{-\tau(q)} \tag{3}$$

where $\tau(q)$ can be obtained from the slope of the double logarithmic curve of $\chi(q, \varepsilon)$ versus ε.

(4) The generalized fractal dimension D_q. D_q is related to $\tau(q)$ as follows [53]:

$$\tau(q) = (q-1)D_q \tag{4}$$

In combination with Equations (3) and (4), the D_q can be given by:

$$D_q = \lim_{\varepsilon \to 0} \frac{1}{q-1} \frac{\log[\chi(q, \varepsilon)]}{\log(\varepsilon)} \tag{5}$$

where $q \neq 1$. For $q = 1$, D_1 can be obtained by L'Hôpital rule [51]:

$$D_1 = \lim_{\varepsilon \to 0} \frac{\sum_{i=1}^{N(\varepsilon)} \chi_i(1, \varepsilon) \log[\chi_i(1, \varepsilon)]}{\log(\varepsilon)} \tag{6}$$

The D_q values at $q = 0$, $q = 1$, and $q = 2$ are named capacity dimension D_0, information dimension D_1, and correlation dimension D_2, respectively. For monofractal, $D_0 = D_1 = D_2$ and the D_q spectrum is a horizontal line. For multifractal, the D_q spectrum is a monotonically decreasing function of q and $D_0 > D_1 > D_2$. According to Riedi et al. [54], D_2 can be replaced by Hurst exponent H as:

$$D_2 = 2H - 1 \tag{7}$$

where H indicates the autocorrelation of pore volume distribution over the set of pore sizes related to long-range spatial variation [36,51,55].

3. Results and Discussion

3.1. TOC Content and Mineral Compositions of Shale Samples

The TOC contents and mineral compositions of the shale samples are listed in Table 1. The TOC values vary from 0.396% to 2.417%, with an average value of 1.285%. This means both the organic-rich and organic-poor shale samples can be identified. Furthermore, previous studies [56–60] have generally categorized the shale types based on the contents of siliceous minerals (quartz and feldspar) and carbonate and clay minerals from XRD analysis. Thus, the studied shale samples can be classified into three types, as presented in the ternary plot (Figure 2), namely carbonate and mixed and argillaceous shales. This is consistent with the findings by He et al. [13], who have categorized the primary types of Ziliujing shales into the same three groups based on XRD results of 70 samples. Hence, the 12 samples chosen are considered to be representative of the studied interval in the reservoir. For carbonate shales, the calcite contents are larger than 50%, while both the contents of quartz and clay are less than 20% (Table 1). The contents of calcite, quartz, and clay in mixed shales are close, within the ranges of 26.9–35.3%, 27.8–30.7%, and 28.2–29.5%, respectively (Table 1). For argillaceous shales, the clay contents are higher than 50% (51.2–59.0%), and the quartz contents vary from 26.3% to 29.6%, while calcite contents are below 5% (Table 1). The mineral compositions of different samples show a significant impact on pore distributions and pore heterogeneity, which will be discussed in the following Section 3.3.
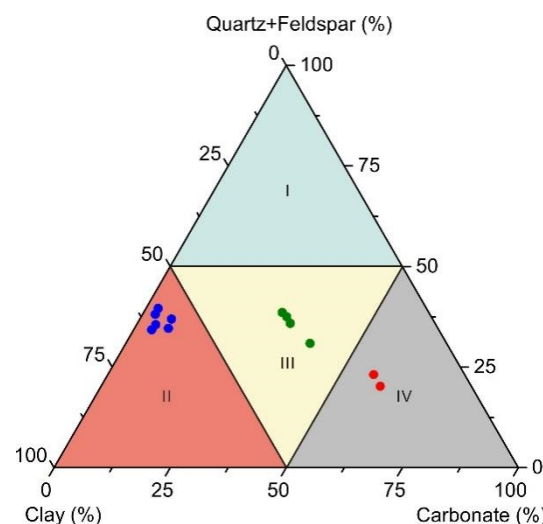

Figure 2. Mineral composition characteristics of the shale samples. (I: siliceous shales; II: argillaceous shales; III: mixed shales; IV: carbonate shales. The red dots represent carbonate shales, the green dots represent mixed shales, and the blue dots represent argillaceous shales).

The QEMSCAN images of the three typical types of shales can be seen in Figure 3. The carbonate shale (sample D97) is mainly composed of calcite (65.18%) with scarce organic matter (0.47%) (Figure 3a). This result is consistent with the XRD analysis. However, the content of quartz from QEMSCAN in sample D97 is only 7.9%, which is less than that obtained from XRD analysis. The heterogeneity of shale is strong at the nano and micro scale, which means, in comparison to QEMSCAN, XRD analysis of the power samples will be more accurate and free from such heterogeneity. In this regard, QEMSCAN can directly observe the distributions of mineral compositions, except for the quantitative contents of minerals. For carbonate shale (Figure 3a), the calcites exhibit a layered structure with illite embedded in calcite particles, and the pyrite aggregates are randomly distributed in the samples. In terms of the mixed shale (sample D123), the clay and quartz contents are 29.45% and 28.93%, respectively (Figure 3b), while the clay and quartz contents of the argillaceous shale (sample D71) with a lesser amount of calcite (3.80%) is 50.38% and 23.85%, respectively (Figure 3c). Both the mixed and argillaceous shales exhibit dense massive textures, which demonstrates an ultralow porosity and permeability in the shale samples should be expected.
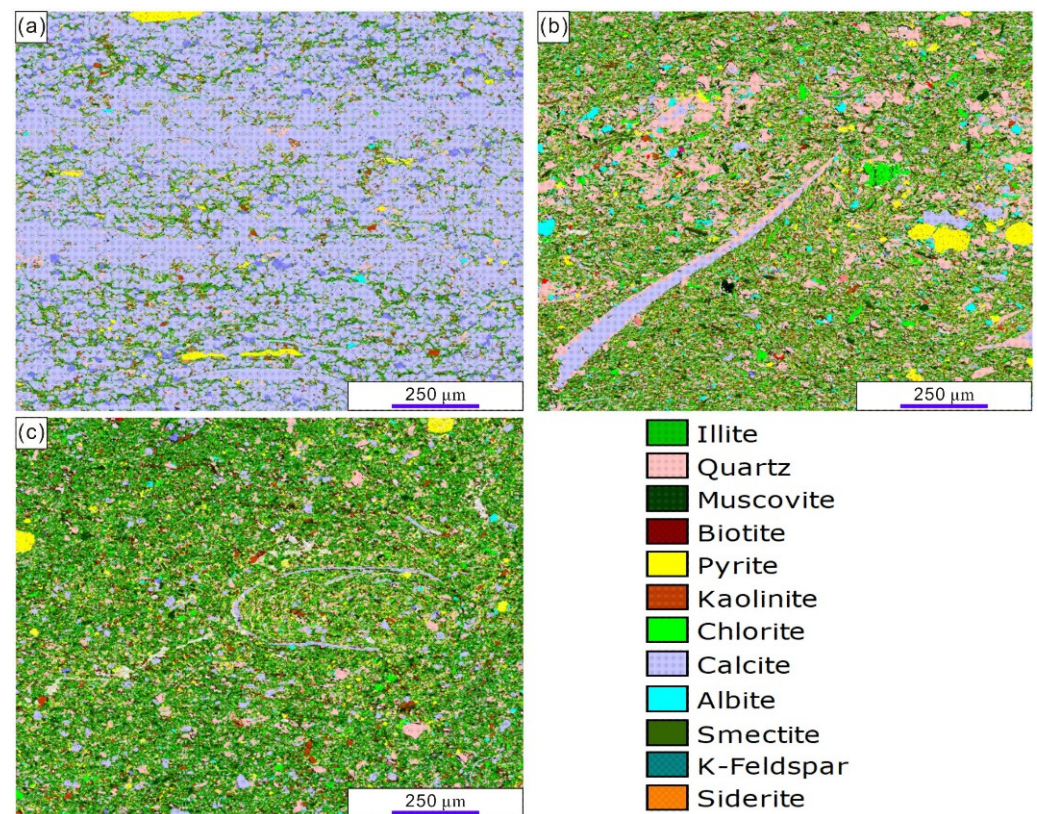

Figure 3. QEMSCAN images of different types of shale samples. (**a**) the carbonate shale of sample D97, (**b**) the mixed shale of sample D123, (**c**) the argillaceous shale of sample D71.

3.2. Meso- and Macropore Characteristics of the Shale Samples

Figure 4 shows the low-temperature N_2 adsorption/desorption isotherms of the shale samples. According to the gas adsorption classification [61], the isotherms of all the samples belong to type IV curves. The desorption isotherms of all the samples are located in the upper part of the adsorption isotherms, and a clear inflection point occurs at a relative pressure of 0.5, where the adsorption hysteresis occurs. The types of the adsorption hysteresis loop can be used to determine the pore shape of the adsorbent [62]. The adsorption hysteresis loops of all the samples are of H3 type (Figure 4), suggesting that the pore morphology is dominated by wide slit-type pores. However, there are obvious differences in the N_2 adsorption amounts of different types of shales. The N_2

adsorption values of both carbonate and mixed shales are less than 11 cm^3/g (Figure 4a), while those of argillaceous shales are higher than 15 cm^3/g (Figure 4b). The variations of N$_2$ adsorption amounts indicate that obvious differences exist in the pore structure of different shale samples. The pore structure parameters of the shale samples derived from the low-temperature N$_2$ adsorption/desorption isotherms are presented in Table 2.
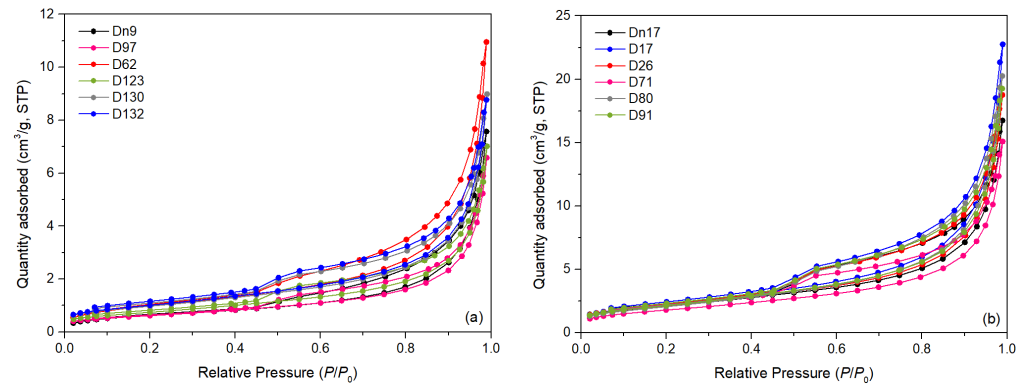

Figure 4. Low-temperature N$_2$ adsorption/desorption isotherms of the shale samples. (**a**) LNA curves of carbonate and mixed shale samples, (**b**) LNA curves of argillaceous shale samples.

Table 2. Pore parameters of the shale samples derived from LNA methods.

Samples	Shale Type	S_{BET} (m^2/g)	Pore Volume (cm^3/g)			APS (nm)
			V_T	V_{meso}	V_{macro}	
Dn9	carbonate	2.32	0.0125	0.0083	0.0041	14.01
D97		2.23	0.0109	0.0073	0.0036	14.99
D62	mixed	3.68	0.0181	0.0124	0.0057	12.07
D123		2.71	0.0115	0.0075	0.0041	11.43
D130		3.50	0.0146	0.0094	0.0052	11.97
D132		3.66	0.0143	0.0099	0.0044	11.03
Dn17	argillaceous	7.46	0.0277	0.0206	0.0071	10.09
D17		8.07	0.0376	0.0265	0.0111	11.98
D26		7.62	0.0310	0.0227	0.0083	10.92
D71		6.48	0.0246	0.0181	0.0065	10.15
D80		7.52	0.0338	0.0254	0.0085	11.27
D91		7.77	0.0319	0.0237	0.0083	10.85

Note: V_T—total pore volume; V_{meso}—mesopore volume (2–50 nm); V_{macro}—macropore volume (>50 nm); APS—average pore size.

As shown in Table 2, the mesopore volume of all the samples is higher than the macropore volume. This change is similar to the pore variations in samples from the Longmaxi Formation [22,35]. However, there are clear differences in the pore parameters of different types of shales. The carbonate shales exhibited the lowest SSA (2.23–2.32 m^2/g) and PV (0.0109–0.0125 cm^3/g) but the largest APD (14.50 nm on average). Compared with carbonate shale, the SSA and PV of mixed shales were found to increase by 1.13 m^2/g and 0.003 cm^3/g on average, respectively, and the meso- and macropore volumes increased by 25.46% and 25.08%, respectively, while the APD decreased to 11.62 nm on average. The SSA and PV of argillaceous shales showed a significant increase within the ranges of 6.48–8.07 m^2/g and 0.0246–0.0376 cm^3/g, respectively. In comparison with mixed shales, the mesopore volume of argillaceous shales increased by 2–4 times, and the macropore volume increased by 71.77% on average, while the APD was found to be the lowest (10.88 nm on average).

The pore size distributions (PSDs) can reveal subtle variations in the pore structure of different shale samples (Figure 5). From Figure 5, the peaks of PSDs of carbonate shales

are concentrated at 9 nm, and the porosity is found between 2 nm and 30 nm. The PSDs of mixed shales become wider, while the peaks are left shifted to 3.4 nm. Except for the D123 sample, the number of pores with a diameter of less than 35 nm of mixed shales increased significantly, resulting in an increased mesopore volume and SSA. The pore number with a diameter less than 8 nm in D123 samples increased, but the opposite trend is recorded for pore diameter >8 nm. As a result, the meso- and macroporosity increased slightly. The PSDs of argillaceous shales are similar to those of mixed shales. However, the PV in the whole pore size range of clay shales increased, especially for the pores with size <30 nm. Thus, the mesopore volume and SSA sharply increased, but the APD decreased. The results indicate that the increase in mesopore volume of continental shale will prompt the formation of pores with small size and enlarged SSA, which is consistent with the previous studies [16,22,35].
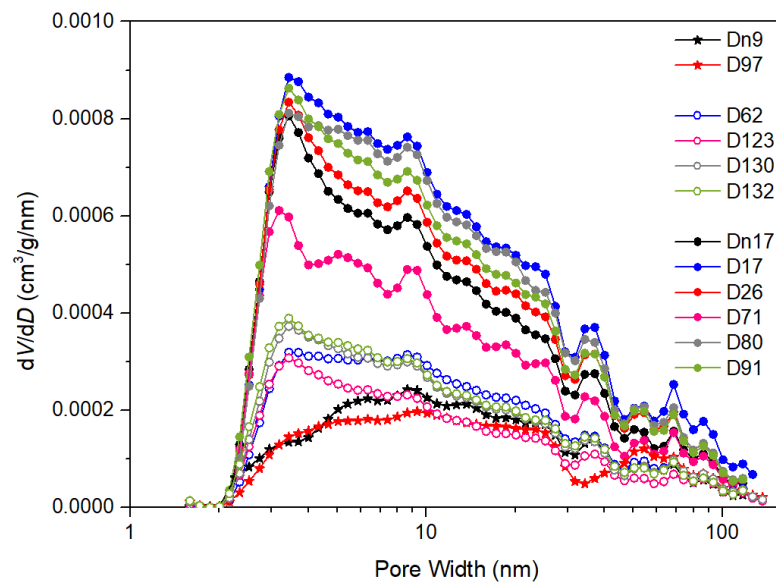

Figure 5. Pore size distributions of the shale samples derived from N_2 adsorption methods.

3.3. Effect of Mineral Compositions on Meso- and Macropore Structures

Many studies have shown that mineral compositions and TOC are the main factors that would affect shale pore structure parameters [16,22,63,64]. Figure 6 depicts the relationship between the mineral compositions with SSA, V_T, V_{meso}, and V_{macro}. A strong positive correlation can be seen between clay mineral contents and SSA, TPV, V_{meso}, and V_{macro}. All the complex correlation coefficients, R^2, are greater than 0.89 (Figure 6(a_1,a_2)). Nevertheless, a significant negative correlation ($R^2 > 0.70$) is observed between carbonate content and the above pore parameters (Figure 6(b_1,b_2)). Furthermore, we did not observe any clear relationship between the amounts of quartz and feldspar (QF) and pore parameters (Figure 6(c_1,c_2)). As described in Figure 6(a_2,b_2), the variations of R^2 demonstrate that the influence of clay and carbonate on V_{meso} is greater than that on V_{macro}. The mentioned results illustrate that clay and carbonate mineral content are the main factors affecting meso- and macropore distributions, but negatively. Previous works [22,27,35,43] have stated that shales with high clay mineral content generally own high meso- and macropore volumes. In this regard, Rexer et al. [65] explained that carbonate precipitation would hinder pore development, which means the higher the content of carbonate minerals, the lower the volume of mesopores and macropores should be. In this study, the amounts of QF among different shale samples were found to be similar, which leads to a very weak correlation between QF and pore parameters.
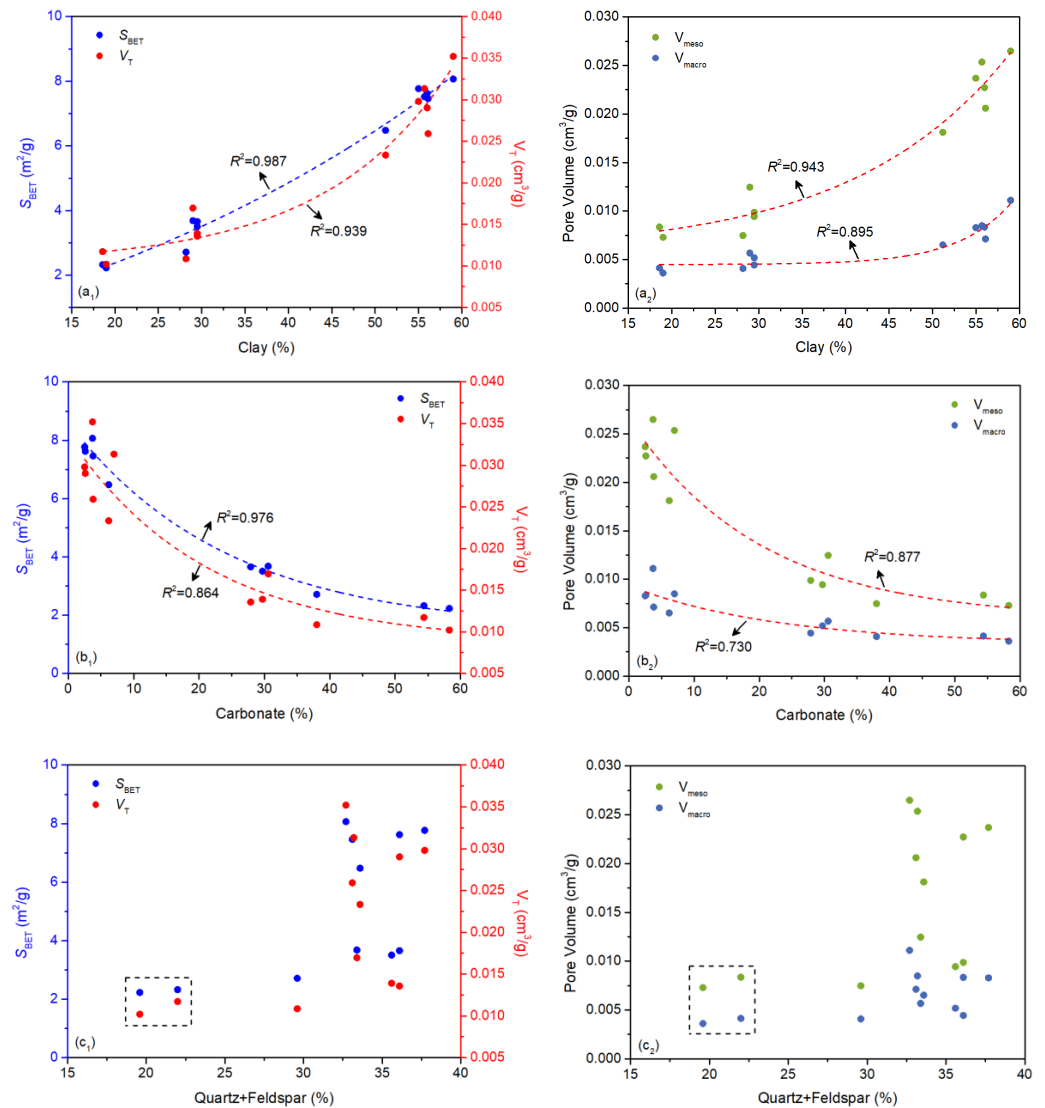
Figure 6. Relationships of mineral compositions and SSA, TPV, V_{meso}, and V_{macro}. (a_1–c_1) Relationships of clay, carbonate, and QF with SSA and TPV, respectively. (a_2–c_2) Relationships of clay, carbonate, and QF with meso- and macropore volumes, respectively. (Dotted boxes represent pore parameters of carbonate shales).

The relationships between TOC and SSA and pore volume are plotted in Figure 7. Ambrose et al. [66] found that TOC played an important role in the distributions of PV and SSA. Liu et al. [67] analyzed the relationships of TOC with V_{meso} and V_{macro} of continental shales from the Yanchang Formation in the Ordos Basin by low-temperature N_2 adsorption method. They found that TOC encouraged the development of V_{meso}, V_{macro}, and SSA. Similar trends were observed in marine shales by Wu et al. [68]. However, no correlations can be observed here between TOC and pore parameters. Jiang et al. [22] considered that the weak correlations between TOC and pore parameters might originate from six different factors, that is, organic matter preservation process to form TOC, organic matter biogenic origin, thermal maturity, intercrystalline pores between pyrites, secondary enlargement of quartz, and the occurrence of irreducible fluids. Therefore, the ambiguous relationships between TOC and pore parameters from N_2 adsorption might be due to multiple factors that need further study.
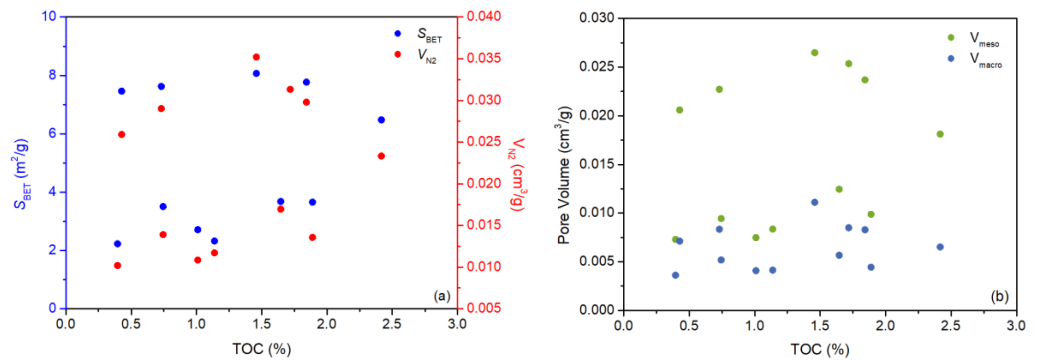
Figure 7. Relationships of TOC with SSA, V_T, V_{meso}, and V_{macro}. (**a**) Relationships of TOC with SSA and V_T, respectively. (**b**) Relationships of TOC with V_{meso} and V_{macro}, respectively.

3.4. Multifractal Characteristics of Meso- and Macropore Structures

According to Equations (1)–(6), the generalized dimension spectra (D_q vs. q) of the shale samples in the range of moment $q = -10$ to $q = 10$ are plotted in Figure 8. The relevant multifractal parameters are listed in Table 3. It can be seen that the D_q spectra of all the samples are monotonically decreasing as a function of q, and $D_0 > D_1 > D_2$. The results suggest that the pore size distributions of meso- and macropores of shales exhibit multifractal behavior. According to multifractal theory, it is known that the generalized spectra D_q and the corresponding characteristic parameters can describe the inner complexity or heterogeneity in the size-dependent distribution of pore volume [36,51].
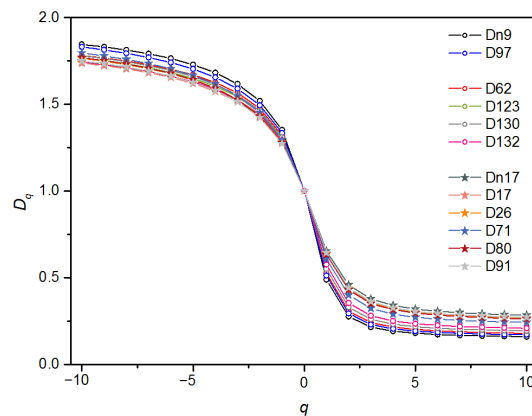

Figure 8. Generalized dimension D_q, versus q from $q = -10$ to $q = +10$ for PSDs of the shale samples.

Table 3. Multifractal parameters of pores derived from N_2 adsorption isotherms for shale samples.

Shales	Samples	D_0	D_1	H	D_{10}	D_{-10}	D_0-D_{10}	$D_{-10}-D_0$	$D_{-10}-D_{10}$
carbonate	Dn9	1.000	0.489	0.638	0.160	1.846	0.840	0.846	1.686
	D97	1.000	0.512	0.647	0.171	1.831	0.829	0.831	1.660
mixed	D62	1.000	0.526	0.654	0.179	1.781	0.821	0.781	1.602
	D123	1.000	0.552	0.665	0.193	1.768	0.807	0.768	1.575
	D130	1.000	0.551	0.665	0.193	1.781	0.807	0.781	1.588
	D132	1.000	0.575	0.677	0.208	1.743	0.792	0.743	1.535
argillaceous	Dn17	1.000	0.655	0.729	0.284	1.748	0.716	0.748	1.464
	D17	1.000	0.638	0.717	0.264	1.738	0.736	0.738	1.474
	D26	1.000	0.638	0.719	0.269	1.765	0.731	0.765	1.496
	D71	1.000	0.609	0.700	0.242	1.796	0.758	0.796	1.554
	D80	1.000	0.634	0.715	0.263	1.796	0.737	0.796	1.533
	D91	1.000	0.643	0.721	0.272	1.750	0.728	0.750	1.478

As seen in Figure 8 and Table 3, the multifractal characteristics of pores in different types of shales demonstrate significant discrepancies. The D_q spectra morphology and the width D_{-10}–D_{10} depict the variability of local porosity along the pore size intervals [53]. The wider the D_q spectra, the greater the local fluctuation in PSDs and the higher the complexity in pore structure. The carbonate shales exhibited the largest curvature of D_q spectra (Figure 8) and the largest values of D_{-10}–D_{10} (Table 3), indicating that carbonate minerals increase the multifractality of PSDs as well as the complexity of pore structure. The average values of D_{-10}–D_{10} for mixed and argillaceous shales are 1.575 and 1.499, respectively, denoting a higher degree of heterogeneity in PSDs of mixed shales.

Figure 8 shows that the left branches in D_{-10}–D_0 of the mixed shales and argillaceous shales are crossed and overlapped and cannot be distinguished well. However, the right branch D_0–D_{10} of the argillaceous shale is located above the mixed shales, and the D_q values of the right branch of carbonate shales are the smallest (Figure 8). As listed in Table 3, the D_0–D_{10} values of carbonate shales are greater than 0.82, and the average values for mixed shales and argillaceous shales are 0.81 and 0.72, respectively. Thus, D_0–D_{10} can be used as an effective parameter to distinguish the inner variations in PSDs of different types of shales. The left and right branches of the D_q spectrum represent different information on the variables. The right branch D_0–D_{10} ($q > 0$) and the left branch D_{-10}–D_0 ($q < 0$) correspond to the dominance of high and low concentrations of pore volume, respectively [36,51]. In combination with Figure 5, the pore volume distributions with size <50 nm (mesopores) lead to differential distributions among various shale samples. Thus, the right side D_0–D_{10} for $q > 0$ reflects the various distributions of mesopores and the left side D_{-10}–D_0 for $q < 0$ represents the inner complexity in the distribution of macropores.

D_1 and H characterize the concentration of PSDs and the autocorrelation of pore connectivity, respectively [36,51]. The smaller D_1 and H, the greater the fluctuation in the inner distributions of pores would be, the narrower the PSDs, and the lower pore connectivity along pore size intervals should be expected. On the contrary, uniformity in the PSDs in each pore size interval and stronger connectivity among different pore size intervals can be understood. The D_1 and H values of carbonate shale are the smallest, indicative of concentrated PSDs. This is compatible with the results in Section 3.3. Compared with carbonate shale, the D_1 and H values of mixed shales increased, varying from 0.52–0.58 and 0.65–0.68, respectively. This infers weakened pore clustering and enhanced pore connectivity. Combined with Figure 5, the pore volume with a size less than 10 nm in mixed shale obviously increased, thus widening the PSDs and enhancing the connectivity between the pores. As a result, the values of D_1 and H increase. The D_1 and H values of argillaceous shales continue to increase with the average values of 0.64 and 0.72, respectively. The results show that argillaceous shales have a relatively homogeneous distribution of pore volume over different pore diameter intervals. The PSDs of argillaceous shales in Figure 5 suggest that the rapid increase in mesopore volume may be attributed to the strong autocorrelation and pore connectivity among the pore size range, which is the main reason for the difference in D_1 and H of different types of shales.

3.5. Relationships of Pore Parameters, Mineral Compositions, TOC, and Multifractal Parameters from N$_2$ Adsorption

The correlations of pore parameters (V_T, V_{meso}, V_{macro}), mineral compositions, TOC, and multifractal parameters were conducted by a linear regressive analysis (Table 4). At the $p = 0.01$ level, V_T, V_{meso}, V_{macro}, and clay show strong linear positive correlations to D_1 and H and negative correlations to D_0–D_{10} ($R > 0.8$). On the contrary, carbonate content displays a strongly negative correlation to D_1 and H and a positive correlation to D_0–D_{10} ($R > 0.9$). QF also exhibits some positive or negative correlation to the above-mentioned multifractal parameters, although the degree of correlation decreases with correlation coefficients R ranging from 0.582–0.645 at the $p = 0.1$ level. V_T, V_{meso}, V_{macro}, and QF exhibit strong negative correlations to D_{-10}–D_{10} at the $p = 0.05$ level, while carbonate and clay are positively and negatively correlated to D_{-10}–D_{10} at the $p = 0.01$ level, respectively.

A lower correlation ($0.392 < R < 0.525$) can be found between V_T, V_{meso}, V_{macro}, and clay and D_{-10}–D_0. Carbonate shows a somewhat positive correlation to D_{-10}–D_0 at the $p = 0.1$ level, while a strong negative correlation exists between QF and D_{-10}–D_0. Moreover, a weak relationship between TOC and multifractal parameters is recorded ($0.394 < R < 0.442$).

Table 4. Relationships of V_T, V_{meso}, V_{macro}, mineral compositions, TOC, and multifractal parameters.

	D_1	H	D_0–D_{10}	D_{-10}–D_{10}	D_{-10}–D_0
V_T	0.875 **	0.893 **	−0.895 **	−0.782 *	−0.414
V_{meso}	0.886 **	0.906 **	−0.909 **	−0.782 *	−0.392
V_{macro}	0.807 **	0.820 **	−0.819 **	−0.754 *	−0.463
carbonate	−0.952 **	−0.946 **	0.941 **	0.912 **	0.646 †
clay	0.966 **	0.974 **	−0.974 **	−0.879 **	−0.525
QF	0.645 †	0.601 †	−0.582 †	−0.744 *	−0.764 *
TOC	0.442	0.415	−0.398	−0.416	−0.394

Note: **, significant at $p = 0.01$ confidence level; *, significant at $p = 0.05$ confidence level; †, significant at $p = 0.1$ confidence level.

The multifractal parameters (D_1, H, and D_0–D_{10}) for moment $q > 0$ denote the fractal characteristics of high concentrations of pore volume. As analyzed in Section 3.3, the variations in mesopore volume are the main factor affecting the pore distributions of different shale samples. Consequently, a strongly positive relationship between mesopore volume and multifractal parameters (D_1, H and D_0–D_{10}) for $q > 0$ is observed. The changes in pore distributions and regression results suggest that, in the shale samples studied, the increasing mesopore volume due to increased clay contents is accompanied by lower fluctuation, lower clustering, higher autocorrelation, and lower heterogeneity in the inner size-dependent distribution of pores as indicated by multifractal parameters for $q > 0$. However, the increased carbonate mineral contents play a reverse role.

Although a lower correlation between QF and the multifractal parameters for $q > 0$ exists when compared with clay and carbonate, the increased QF contents contribute to the widening of pore distribution, improve pore connectivity, and reduce the complexity of pore distribution. The multifractal parameters (D_{-10}–D_0) for $q < 0$ describe the complexity of small concentrations of pore volume, which characterizes the inner heterogeneous distribution of macropores. Although the correlation between macropore volume and D_{-10}–D_0 is low, the increasing macropore volume caused by clay mineral content still reduces the complexity in the inner macropore distributions as estimated by the negative correlation coefficient. However, carbonate enhances the complexity and fluctuation of the macropore distributions. In summary, D_1, H, and D_0–D_{10} can be considered to be the parameters that are important to distinguish the internal differences in meso- and macropore distributions along pore size intervals of the Ziliujing shales.

As mentioned above, limited parameters are not enough to demonstrate the multifractal heterogeneity of macropores. Previous research [69,70] showed that the pore size range of shale oil reservoirs varied from nanometers to millimeters, and the pores with a diameter larger than 100 nm (seepage-pores) are crucial to the transport and development of shale oil [71–73]. Thus, it is necessary to fully characterize the pore properties of seepage-pores by the combination of fluid-invasion methods and image analysis techniques, including MIP, low-field nuclear magnetic resonance, micro-CT, SEM, and others. Moreover, further comparison of the multifractal characteristics of pore structure from different methods of shale oil reservoirs is required.

3.6. Comparision of Multifractal Parameters of N$_2$ Adsorption among Different Shale Oil Reservoirs

Figure 9 depicts the comparison of multifractal parameters of N$_2$ adsorption among different shale oil reservoirs. The D_1 values of the Bakken shales in the US vary from 0.702 to 0.920, with an average of 0.797 [41]. The Ek2 shales in Cangdong Sag, Bohai Bay Basin, possess the largest D_1 values ranging from 0.927 to 0.982 [44]. The smallest D_1 values are

recorded in the Ziliujing shales, and all the D_1 values are less than 0.7. On the contrary, the largest D_{-10}–D_{10} values can be observed in the Ziliujing shales, and the increasing order for the average value of D_{-10}–D_{10} is followed by Ek2 shales, Bakken shales, and Ziliujing shales. The results indicate that the meso- and macropore structures of the Ziliujing shales are much more heterogeneous than those of the Bakken shales and Ek2 shales.
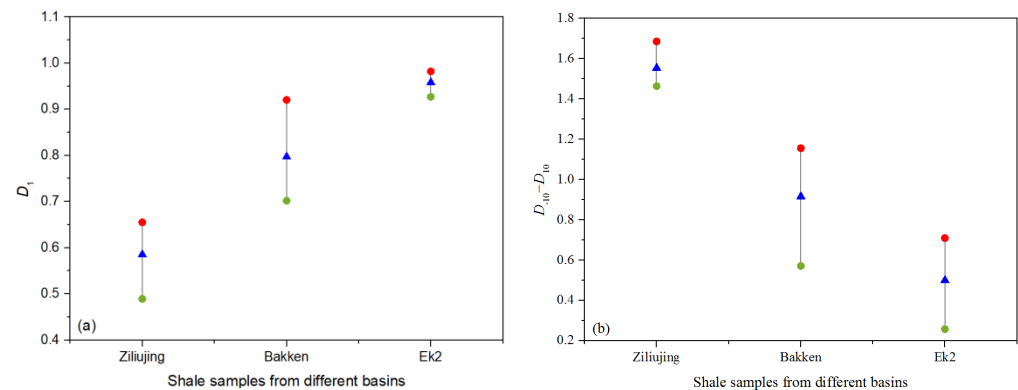

Figure 9. Comparison of multifractal parameters of nanopore heterogeneity of shale oil reservoirs from different basins (**a**) D_1 data of shale samples from different basins. (**b**) D_{-10}–D_{10} data of shale samples from different basins. (The red circle represents the maximum value, the green circle represents the minimum value, and the blue triangle represents the average value. The D_1 and D_{-10}–D_{10} data of the Bakken shale from Liu et al. [41], and the D_1 and D_{-10}–D_{10} data of the Ek2 shale from Guan et al. [44]).

The reasons for this discrepancy of nanopore heterogeneity of the shale oil reservoirs in different basins can be attributed to thermal maturity (R_o), mineral compositions, sedimentary environment, etc. [41,44]. Guan et al. [44] illustrated that the nanopore complexity subsequently increased when R_o is greater than 0.65%. Both the R_o of the Bakken shales from Liu et al. [41] and the Ek2 shales from Guan et al. [44] are less than 1.0%. The R_o of the Ziliujing shales in our study mostly varies from 1.3% to 1.5% [11]. Therefore, compared with the Bakken and Ek2 shales, the higher R_o may tend to increase the meso- and macropore heterogeneity of the Ziliujing shales. The impact on nanopore heterogeneity from inorganic mineral compositions of shale oil reservoirs from different basins is generally a complex inner relation. In this regard, Liu et al. [44] reported that quartz and clay played an opposite effect on the meso- and macropore heterogeneity of the Upper Bakken and Middle Bakken shales, which may be related to depositional sub-facies [70]. Thus, the effect of mineral compositions on nanopore heterogeneity of shale oil reservoirs could vary in different basins. This means that the impact of such components on pore heterogeneity, specifically composition, should be analyzed based on the geological setting and lithofacies in different basins.

4. Conclusions

In this study, the meso- and macropore characteristics of shales of the Ziliujing Formation of the Jurassic age in the Sichuan Basin were investigated by combining low-temperature N_2 adsorption techniques and multifractal method. Based on the results, the conclusions are as follows:

(1) The mineral compositions of the studied Ziliujing shale samples reveal that the shales can be divided into three types: carbonate shale, mixed shale, and argillaceous shale. The calcite contents of carbonate shale were found to be higher than 50%. The differences in calcite, quartz, and clay mineral contents were found to be small for mixed shale. For argillaceous shale, the clay mineral contents were found to be larger than 50%, and the calcite contents were less than 5%.

(2) There are clear differences in meso- and macropore characteristics among different types of shales. The carbonate shale exhibited the lowest specific surface area and pore volume but the largest average pore diameter. The argillaceous shale had the highest specific surface area and pore volume but the smallest average pore size. The pore parameters of the mixed shale were found to be in between. The mesopore volume is the main control of the differential distribution of pores in different types of shales. Clay minerals significantly increased the mesopore contents, while carbonate minerals had the opposite effect. TOC and the combined contents of quartz and feldspar had a weak effect on the pore distributions.

(3) The meso- and macropore distributions of the Ziliujing shales exhibited multifractal behaviors. The information dimension D_1, the Hurst exponent H, and the width of the right side D_0–D_{10} of the D_q spectrum were found effective parameters to distinguish the local variations within the pore distributions of different types of Ziliujing shale samples. As indicated by the change of the multifractal parameters, for the Ziliujing shales studied, clay minerals and quartz and feldspar contents caused a reduction in the pore clustering, enhanced pore connectivity, and weakened the complexity of pore distribution, while carbonate minerals played the opposite role. Therefore, the multifractal approach helps to improve the understanding of internal heterogeneity and differences in meso- and macropore distributions of different types of shales.

(4) A further step is needed to characterize the pores of the Ziliujing shales with sizes varying from nanometers to micrometers in combination with different methods, such as mercury injection and gas adsorption (CO_2 and N_2), an integration of small-angle neutron scattering techniques (SANS and USANS), and micro-CT. Additionally, the analysis of multifractal properties of seepage-pores heterogeneity is necessary, which has implications for permeability calculation, fluid transport, and future development plans.

References

1. Xu, Y.; Lun, Z.M.; Pan, Z.J.; Wang, H.T.; Zhou, X.; Zhao, C.P.; Zhang, D.F. Occurrence space and state of shale oil: A review. *J. Pet. Sci. Eng.* **2022**, *211*, 110183. [CrossRef]
2. Yu, Y.J.; Wang, H.Y.; Liu, D.X.; Zhao, Q.; Li, X.B.; Wu, J.; Xia, Z.Y. Development Status and Feasibility Evaluation Index System of Continental Shale Oil Demonstration Area in China. *Earth Sci.* **2023**, *48*, 191–205. (In Chinese with English abstract)
3. Zou, C.N.; Ma, F.; Pan, S.Q.; Zhang, X.S.; Wu, S.T.; Fu, G.Y.; Wang, H.J.; Yang, Z. Formation and distribution potential of global shale oil and the development of continental shale oil theory and technology in China. *Earth Sci. Front.* **2023**, *30*, 128–142. (In Chinese with English abstract)

4. Du, J.H.; Hu, S.Y.; Pang, Z.L.; Lin, S.H.; Hou, L.H.; Zhu, R.K. The types, potentials and prospects of continental shale oil in China. *China Pet. Explor.* **2019**, *24*, 560–568. (In Chinese with English abstract)

5. Jin, Z.Y.; Wang, G.P.; Liu, G.X.; Gao, B.; Liu, Q.Y.; Wang, H.L.; Liang, X.P.; Wang, R.Y. Research progress and key scientific issues of continental shale oil in China. *Acta Pet. Sin.* **2021**, *42*, 821–835. (In Chinese with English abstract)

6. Sun, L.D.; He, W.Y.; Feng, Z.H.; Zeng, H.S.; Jiang, H.; Pan, Z.J. Shale oil and gas generation process and pore fracture system evolution mechanisms of the continental Gulong Shale, Songliao Basin, China. *Energy Fuels* **2022**, *36*, 6893–6905. [CrossRef]

7. Guo, Q.L.; Pan, S.Q.; Yang, F.; Yao, Y.; Zheng, H. Characterizing shale oil occurrence in the Yanchang formation of the Ordos Basin, Assisted by Petrophysical and Geochemical Approaches. *Energy Fuels* **2022**, *36*, 370–381. [CrossRef]

8. Lv, J.H.; Jiang, F.J.; Hu, T.; Zhang, C.X.; Huang, R.D.; Hu, M.L.; Xue, J.; Huang, L.L.; Wu, Y.P. Control of complex lithofacies on the shale oil potential in ancient alkaline lacustrine basins: The Fengcheng Formation, Mahu Sag, Junggar basin. *Geoenergy Sci. Eng.* **2023**, *224*, 211501. [CrossRef]

9. Zhi, D.M.; Xiang, B.L.; Zhou, N.; Li, E.T.; Zhang, C.J.; Wang, Y.C.; Cao, J. Contrasting shale oil accumulation in the upper and lower sweet spots of the lacustrine Permian Lucaogou Formation, Junggar Basin, China. *Mar. Pet. Geol.* **2023**, *150*, 106178. [CrossRef]

10. Meng, M.M.; Peng, J.C.; Ge, H.K.; Ji, W.M.; Li, X.M.; Wang, Q.Y. Rock fabric of lacustrine shale and its influence on residual oil distribution in the Upper Cretaceous Qingshankou Formation, Songliao Basin. *Energy Fuels* **2023**, *37*, 7151–7160. [CrossRef]

11. Yang, Y.M.; Yang, J.J.; Yang, G.; Tao, S.Z.; Ni, C.; Zhang, B.; He, X.D.; Lin, J.P.; Huang, D.; Liu, M.; et al. New research progress of Jurassic tight oil in central Sichuan Basin. *Pet. Explor. Dev.* **2016**, *43*, 873–882. (In Chinese with English abstract) [CrossRef]

12. Cheng, S.J.; Zhang, H.X.; Lu, J.G.; Yang, Y.M.; Liu, C.W.; Li, W.; Zou, X.L.; Yang, J.J.; Tang, H.P.; Yao, Y.T.; et al. Controlling factors of Jurassic Da'anzhai Member tight oil accumulation and high production in central Sichuan Basin, SW China. *Pet. Explor. Dev.* **2015**, *42*, 186–193. (In Chinese with English abstract)

13. Wenyuan, H.; Xuefeng, B.A.; Qi'an, M.; Junhui, L.; Dazhi, Z.; Youzhi, W. Accumulation geological characteristics and major discoveries of lacustrine shale oil in Sichuan Basin. *Acta Pet. Sin.* **2022**, *43*, 885–898. (In Chinese with English abstract)

14. Li, Z.; Lei, Z.; Shen, W.; Martyushev, D.A.; Hu, X. A comprehensive review of the oil flow mechanism and numerical simulations in shale oil reservoirs. *Energies* **2023**, *16*, 3516. [CrossRef]

15. Liu, B.; Wang, Y.; Tian, S.S.; Guo, Y.L.; Wang, L.; Yasin, Q.; Yang, J.G. Impact of thermal maturity on the diagenesis and porosity of lacustrine oil-prone shales: Insights from natural shale samples with thermal maturation in the oil generation window. *Int. J. Coal Geol.* **2022**, *261*, 104079. [CrossRef]

16. Chalmers, G.R.; Bustin, R.M.; Power, I.M. Characterization of gas shale pore systems by porosimetry, pycnometry, surface area, and field emission scanning electron microscopy transmission electron microscopy image. *AAPG Bull.* **2012**, *96*, 1099–1119. [CrossRef]

17. Martyushev, D.A.; Ponomareva, I.N.; Osovetsky, B.M.; Kazymov, K.P.; Tomilina, E.M.; Lebedeva, A.S.; Chukhlov, A.S. Study of the structure and development of oil deposits in carbonate reservoirs using field data and X-ray microtomography. *Georesursy* **2022**, *24*, 114–124.

18. Sun, M.D.; Zhao, J.L.; Pan, J.Z.; Hu, Q.H.; Yu, B.S.; Tan, Y.L.; Sun, L.W.; Bai, L.F.; Wu, C.M.; Blach, T.P.; et al. Pore characterization of shales: A review of small angle scattering technique. *J. Nat. Gas Sci. Eng.* **2020**, *78*, 103294. [CrossRef]

19. Meng, M.; Ge, H.; Shen, Y.; Ji, W.; Li, Z. Insight into water occurrence and pore size distribution by nuclear magnetic resonance in marine shale reservoirs, southern China. *Energy Fuels* **2023**, *37*, 319–327. [CrossRef]

20. Martyushev, D.A.; Ponomareva, I.N.; Chukhlov, A.S.; Davoodi, S.; Osovetsky, B.M.; Kazymov, K.P.; Yang, Y. Study of void space structure and its influence on carbonate reservoir properties: X-ray microtomography, electron microscopy, and well testing. *Mar. Pet. Geol.* **2023**, *151*, 106192. [CrossRef]

21. Liu, Q.; Sun, M.D.; Sun, X.D.; Liu, B.; Ostadhassan, M.; Huang, W.X.; Chen, X.X.; Pan, Z.J. Pore network characterization of shale reservoirs through state-of-the-art X-ray computed tomography: A review. *Gas Sci. Eng.* **2023**, *113*, 204967. [CrossRef]

22. Jiang, F.J.; Chen, D.; Wang, Z.F.; Xu, Z.Y.; Chen, J.; Liu, L.; Huyan, Y.Y.; Liu, Y. Pore characteristic analysis of a lacustrine shale: A case study in the Ordos Basin, NW China. *Mar. Pet. Geol.* **2016**, *73*, 554–571. [CrossRef]

23. Zhao, J.H.; Jin, Z.J.; Hu, Q.H.; Jin, Z.K.; Barber, T.J.; Zhang, Y.X.; Bleuel, M. Integrating SANS and fluid-invasion methods to characterize pore structure of typical American shale oil reservoirs. *Sci. Rep.* **2017**, *7*, 15413. [CrossRef]

24. Zhang, P.F.; Lu, S.F.; Li, J.Q. Characterization of pore size distributions of shale oil reservoirs: A case study from Dongying sag, Bohai Bay basin, China. *Mar. Pet. Geol.* **2019**, *100*, 297–308. [CrossRef]

25. Hou, L.H.; Wu, S.T.; Jing, Z.H.; Jiang, X.H.; Yu, Z.C.; Hua, G.L.; Su, L.; Yu, C.; Liao, F.R.; Tian, H. Effects of types and content of clay minerals on reservoir effectiveness for lacustrine organic matter rich shale. *Fuel* **2022**, *327*, 125043. [CrossRef]

26. Zheng, H.; Yang, F.; Guo, Q.L.; Pan, S.Q.; Jiang, S.; Wang, H. Multi-scale pore structure, pore network and pore connectivity of tight shale oil reservoir from Triassic Yanchang Formation, Ordos Basin. *J. Pet. Sci. Eng.* **2022**, *212*, 110283. [CrossRef]

27. Clarkson, C.R.; Solano, N.; Bustin, R.M.; Bustin, A.M.M.; Chalmers, G.R.L.; He, L.; Melnichenko, Y.B.; Radliński, A.P.; Blach, T.P. Pore structure characterization of North American shale gas reservoirs using USANS/SANS, gas adsorption, and mercury intrusion. *Fuel* **2013**, *103*, 606–616. [CrossRef]

28. Mastalerz, M.; Hampton, L.; Drobniak, A.; Loope, H. Significance of analytical particle size in low-pressure N_2 and CO_2 adsorption of coal and shale. *Int. J. Coal Geol.* **2017**, *178*, 122–131. [CrossRef]

29. Yang, F.; Ning, Z.F.; Liu, H.Q. Fractal characteristics of shales from a shale gas reservoir in the Sichuan Basin, China. *Fuel* **2014**, *115*, 378–384. [CrossRef]

30. Liang, L.X.; Xiong, J.; Liu, X.J. An investigation of the fractal characteristics of the Upper Ordovician Wufeng Formation shale using nitrogen adsorption analysis. *Mar. Pet. Geol.* **2015**, *27*, 402–409. [CrossRef]

31. Sun, L.N.; Tuo, J.C.; Zhang, M.F.; Wu, C.J.; Chai, S.Q. Pore structures and fractal characteristics of nano-pores in shale of Lucaogou formation from Junggar Basin during water pressure-controlled artificial pyrolysis. *J. Anal. Appl. Pyrolysis* **2019**, *140*, 404–412. [CrossRef]

32. Martyushev, D.A.; Chalova, P.O.; Davoodi, S.; Ashraf, U. Evaluation of facies heterogeneity in reef carbonate reservoirs: A case study from the oil field, Perm Krai, Central-Eastern Russia. *Geoenergy Sci. Eng.* **2023**, *227*, 211814. [CrossRef]

33. Friesen, W.I.; Mikula, R.J. Mercury porosimetry of coals: Pore volume distribution and compressibility. *Fuel* **1988**, *67*, 1516–1520. [CrossRef]

34. Wang, M.; Xue, H.T.; Tian, S.S.; Wilkins, R.W.T.; Wang, Z.W. Fractal characteristics of upper Cretaceous lacustrine shale from the Songliao Basin, NE China. *Mar. Pet. Geol.* **2015**, *67*, 144–153. [CrossRef]

35. Yang, R.; He, S.; Yi, J.Z.; Hu, Q.H. Nano-scale pore structure and fractal dimension of organic-rich Wufeng-Longmaxi shale from Jiaoshiba area, Sichuan Basin Investigations using FE-SEM, gas adsorption and helium pycnometry. *Mar. Pet. Geol.* **2016**, *70*, 27–45. [CrossRef]

36. Guan, M.; Liu, X.P.; Jin, Z.J.; Lai, J.; Sun, B.; Zhang, P.P.; Chen, K.F. The evolution of pore structure heterogeneity during thermal maturation in lacustrine shale pyrolysis. *J. Anal. Appl. Pyrolysis* **2022**, *163*, 105501. [CrossRef]

37. Lopes, P.; Betrouni, F. Fractal and multifractal analysis: A review. *Med. Image Anal.* **2009**, *13*, 634–649. [CrossRef]

38. Liu, K.Q.; Ostadhassan, M. Quantification of the microstructures of Bakken shale reservoirs using multi-fractal and lacunarity analysis. *J. Nat. Gas Sci. Eng.* **2017**, *39*, 62–71. [CrossRef]

39. Zhang, P.F.; Yin, Y.J.; Lu, S.F.; Li, J.Q.; Chang, X.C.; Zhang, J.J.; Pang, Y.M.; Chen, G.; Liu, Y.Q.; Li, Z. Insights into pore structures and multifractal characteristics of shale oil reservoirs: A case study from Dongying Sag, Bohai Bay Basin, China. *Energy Fuels* **2022**, *36*, 8224–8237. [CrossRef]

40. Lu, C.G.; Xiao, X.M.; Xue, Z.Q.; Chen, Z.X.; Li, G.; Feng, Y. Fractal and multifractal characteristics of nanopores and their controlling factors in marine-continental transitional shales and their kerogens from Qinshui Basin, Northern China. *Nat. Resour. Res.* **2023**, *32*, 2313–2336. [CrossRef]

41. Liu, K.; Ostadhassan, M.; Zou, J.; Gentzis, T.; Rezaee, R.; Bubach, B.; Carvajal-Ortiz, H. Multifractal analysis of gas adsorption isotherms for pore structure characterization of the Bakken Shale. *Fuel* **2018**, *219*, 296–311. [CrossRef]

42. Liu, K.Q.; Ostadhassan, M.; Gentzis, T.; Fowler, H. Image analysis of the pore structures: An intensive study for Middle Bakken. *J. Nat. Gas Sci. Eng.* **2019**, *61*, 32–45. [CrossRef]

43. Zhang, P.F.; Lu, S.F.; Li, J.Q.; Chang, X.C.; Li, J.J.; Li, W.B.; Chen, G.; Wang, S.Y.; Feng, W.J. Broad ion beam-scanning electron microscopy pore microstructure and multifractal characterization of shale oil reservoir: A case sample from Dongying sag, Bohai Bay basin, China. *Energy Explor. Exploit.* **2020**, *38*, 613–628. [CrossRef]

44. Guan, M.; Liu, X.P.; Jin, Z.J.; Lai, J. The heterogeneity of pore structure in lacustrine shales: Insights from multifractal analysis using N_2 adsorption and mercury intrusion. *Mar. Pet. Geol.* **2020**, *114*, 104150. [CrossRef]

45. Bai, X.F.; Huang, S.P.; Wang, X.D.; Wang, Z.G.; Wang, Y.Z.; Ma, W.Q.; Zhu, Y.P.; Sun, M.D.; Liu, B.; Cheng, L.J.; et al. Microscopic Analysis of Natural Fracture Properties in Organic-Rich Continental Shale Oil Reservoirs: A Case Study from the Lower Jurassic in the Sichuan Basin, China. *J. Mar. Sci. Eng.* **2023**, *11*, 1036. [CrossRef]

46. *GB/T 19145–2003*; Determination of total organic carbon in sedimentary. General Administration of Quality Supervision, Inspection and Quarantine of the People's Republic of China: Beijing, China, 2003.

47. *SY/T 5163–2018*; Analysis Method for Clay Minerals and Ordinary Non-Clay Minerals in Sedimentary Rocks by the X-ray Diffraction. National Energy Administration: Beijing, China, 2018.

48. *SY/T 6189–2018*; Quantitative Analysis Method for Rock Minerals by X-ray Energy Spectrum. National Energy Administration: Beijing, China, 2018.

49. Anovitz, L.M.; Cole, D.R. Characterization and Analysis of Porosity and Pore Structure. *Rev. Miner. Geochem.* **2015**, *80*, 61–164. [CrossRef]

50. Vidal Vázquez, E.; Paz Ferreiro, J.; Miranda, J.G.V.; Paz González, A. Multifractal analysis of pore size distributions as affected by simulated rainfall. *Vadose Zone J.* **2008**, *7*, 500–511. [CrossRef]

51. Li, W.; Liu, H.F.; Song, X.X. Multifractal analysis of Hg pore size distributions of tectonically deformed coals. *Int. J. Coal Geol.* **2015**, *144–145*, 138–152. [CrossRef]

52. Caniego, F.J.; Martín, M.A.; San José, F. Singularity features of pore-size soil distribution: Singularity strength analysis and entropy spectrum. *Fractals* **2001**, *9*, 305–316. [CrossRef]

53. Paz Ferreiro, J.; Vidal Vázquez, E. Multifractal analysis of Hg pore size distributions in soils with contrasting structural stability. *Geoderma* **2010**, *160*, 64–73. [CrossRef]

54. Riedi, R.H.; Crouse, M.S.; Ribeiro, V.J.; Baraniuk, R.G. A multifractal wavelet model with application to network traffic. *IEEE Trans. Inf. Theory* **1999**, *45*, 992–1019. [CrossRef]

55. San José, M.F.; Martín, M.A.; Caniego, F.J.; Tuller, M.; Guber, A.; Pachepsky, Y.; García-Gutiérrez, C. Multifractal analysis of discretized X-ray CT images for the characterization of soil macropore structures. *Geoderma* **2010**, *156*, 32–42. [CrossRef]

56. Wang, G.C.; Carr, T.R. Methodology of organic-rich shale lithofacies identification and prediction: A case study from Marcellus Shale in the Appalachian basin. *Comput. Geosci.* **2012**, *49*, 151–163. [CrossRef]

57. Wang, G.C.; Carr, T.R. Organic-rich Marcellus shale lithofacies modeling and distribution pattern analysis in the Appalachian basin. *AAPG Bull.* **2013**, *97*, 2173–2205. [CrossRef]

58. Guo, X.W.; Qin, Z.J.; Yang, R.; Dong, T.; He, S.; Hao, F.; Yi, J.Z.; Shu, Z.G.; Bao, H.Y.; Liu, K.Y. Comparison of pore systems of clay-rich and silica-rich gas shales in the lower Silurian Longmaxi formation from the Jiaoshiba area in the eastern Sichuan Basin, China. *Mar. Pet. Geol.* **2019**, *101*, 265–280. [CrossRef]

59. Feng, Z.Q.; Zhou, S.W.; Wu, W.; Tian, J.Q.; Xie, C.; Cai, Y.W. Pore characteristics and methane adsorption capacity of different lithofacies of the Wufeng formation-Longmaxi formation shales, Southern Sichuan Basin. *Energy Fuels* **2020**, *34*, 8046–8062. [CrossRef]

60. Xia, P.; Li, H.N.; Fu, Y.; Qiao, W.L.; Guo, C.; Yang, Z.; Huang, J.Q.; Mou, Y.L. Effect of lithofacies on pore structure of the Cambrian organic-rich shale in northern Guizhou, China. *Geol. J.* **2021**, *56*, 1130–1142. [CrossRef]

61. Kruk, M.; Jaroniec, M. Gas Adsorption Characterization of Ordered Organic-Inorganic Nanocomposite Materials. *Chem. Mater.* **2001**, *13*, 3169–3183. [CrossRef]

62. Sing, K.S.W.; Everett, D.H.; Haul, R.A.W.; Moscou, L.; Pierotti, R.A.; Rouquerol, J.; Siemieniewska, T. Reporting physisorption data for gas/solid systems with special reference to the determination of surface area and porosity. *Pure Appl. Chem.* **1985**, *57*, 603–619. [CrossRef]

63. Loucks, R.G.; Reed, R.M.; Ruppel, S.C.; Hammes, U. Spectrum of pore types and networks in mudrocks and a descriptive classification for matrix-related mudrock pores. *AAPG Bull.* **2012**, *96*, 1071–1098. [CrossRef]

64. Bu, H.L.; Ju, Y.W.; Tan, J.Q.; Wang, G.C.; Li, X.S. Fractal characteristics of pores in non-marine shales from the Huainan coalfield, eastern China. *J. Nat. Gas Sci. Eng.* **2015**, *24*, 166–177. [CrossRef]

65. Rexer, T.F.; Mathia, E.J.; Aplin, A.C.; Mark Thomas, K. High-pressure methane adsorption and characterization of pores in Posidonia shales and isolated kerogens. *Energy Fuels* **2014**, *28*, 2886–2901. [CrossRef]

66. Ambrose, R.J. Shale gas-in-place calculations Part I: New pore-scale considerations. *SPE J.* **2012**, *17*, 219–229. [CrossRef]

67. Liu, X.J.; Xiong, J.; Liang, L.X. Investigation of pore structure and fractal characteristics of organic-rich Yanchang formation shale in central China by nitrogen adsorption/desorption analysis. *J. Nat. Gas Sci. Eng.* **2015**, *22*, 62–72. [CrossRef]

68. Wu, J.S.; Yu, B.S.; Zhang, J.C.; Li, Y.X. Pore characteristics and controlling factors in the organic-rich shale of the Lower Silurian Longmaxi Formation revealed by samples from a well in southeastern Chongqing. *Earth Sci. Front.* **2013**, *20*, 260–269.

69. Zhang, P.F.; Lu, S.F.; Li, J.Q.; Chen, C.; Xue, H.T.; Zhang, J. Petrophysical characterization of oil-bearing shales by low-field nuclear magnetic resonance (NMR). *Mar. Pet. Geol.* **2018**, *89*, 775–785. [CrossRef]

70. Liu, K.Q.; Ostadhassan, M.; Sun, L.W.; Zou, J.; Yuan, Y.J.; Gentzis, T.; Zhang, Y.X.; Carvajal-Ortiz, H.; Rezaee, R. A comprehensive pore structure study of the Bakken Shale with SANS, N$_2$ adsorption and mercury intrusion. *Fuel* **2019**, *245*, 274–285. [CrossRef]

71. Yang, R.; Jia, A.Q.; Hu, Q.H.; Guo, X.W.; Sun, M.D. Particle size effect on water vapor sorption measurement of organic shale: One example from Dongyuemiao Member of Lower Jurassic Ziliujing Formation in Jiannan Area of China. *Adv. Geo-Energy Res.* **2020**, *4*, 207–218. [CrossRef]

72. Zhao, J.L.; Sun, M.D.; Pan, Z.J.; Liu, B.; Ostadhassan, M.; Hu, Q.H. Effects of pore connectivity and water saturation on matrix permeability of deep gas shale. *Adv. Geo-Energy Res.* **2022**, *6*, 54–68. [CrossRef]

73. Khurshid, I.; Al-Shalabi, E.W.; Afgan, I.; Al-Attar, H. A numerical approach to investigate the impact of acid-asphaltene sludge formation on Worm-holing during carbonate acidizing. *J. Energy Resour. Technol.* **2022**, *144*, 063001. [CrossRef]